Blob properties in L- and H-mode from gas-puff imaging in ASDEX Upgrade

G. Fuchert[1], G. Birkenmeier[2], D. Carralero[2], T. Lunt[2], P. Manz[4], H. W. Müller[2], B. Nold[3], M. Ramisch[3], V. Rohde[2], U. Stroth[2,4] and the ASDEX Upgrade team

[1] Institut Jean Lamour, Université de Lorraine, CNRS (UMR 7198), BP 70239, 54506 Vandoeuvre-lès-Nancy, France
[2] Max-Planck-Institut für Plasmaphysik, Boltzmannstr. 2, 85748 Garching, Germany
[3] Institut für Grenzflächenverfahrenstechnik und Plasmatechnologie, Universität Stuttgart, 70569 Stuttgart, Germany
[4] Physik-Department E28, Technische Universität München, James-Franck-Str. 1, 85748 Garching, Germany

E-mail: golo.fuchert@univ-lorraine.fr

Abstract.

Blob properties are studied in the scrape-off layer of the tokamak ASDEX Upgrade with a fast camera. The gas-puff imaging technique is used to investigate the detection rate as well as the blob size and velocity scaling. The experiments were performed in L- and H-mode phases of the same discharges to study the change in blob properties after the L-H transition. In both regimes the detection rate is of the order of a few thousand blobs per second, which is compatible with the picture of blob generation by edge micro instabilities. The blob size increases in H-mode, while the radial velocity decreases slightly. The changes are, however, not indicating a drastic change in the blob dynamics in both phases. The experimentally found blob properties were compared to predictions from a novel blob model including effects due to a finite ion temperature, which should be more appropriate for the conditions in the SOL of fusion plasmas.

PACS numbers: 52.25.Xz,52.30.-q,52.35.Ra,52.55.Hc,52.55.Fa

1. Introduction

The discovery of the H-mode [1] was an important step towards the realization of a fusion reactor. The formation of an edge transport barrier leads to an improved confinement and, hence, an increased pressure in the core. H-mode plasmas may provide the conditions required for a self-sustained fusion plasma. In addition to a sufficient energy confinement in the core plasma, however, also the safety of the first wall and the purity of the confined plasma have to be guaranteed. Particle and energy fluxes through the scrape-off layer (SOL) to the walls are increased by plasma turbulence in the edge of fusion plasmas. In the SOL, filamentary structures called "blobs" [2–4] contribute substantially to this turbulent transport [5]. The properties of SOL turbulence and blob dynamics in H-mode plasmas and how they compare with standard L-mode discharges have been studied in a number of fusion experiments [5–10, 39] already. Most of these experiments found only minor differences in the blob dynamics, while others focused more on quantitative differences. In any case these experiments make clear that turbulent transport caused by blobs is an important issue in both confinement regimes.

The amount of transport caused by these blobs depends on their generation rate, cross-field size, and radial velocity [11]. The standard blob models assess these properties by regarding the blob as a filament with a parallel wavenumber of zero ($k_\parallel = 0$), which is polarized by magnetic curvature, causing a poloidal electric field and, hence, radial $\mathbf{E} \times \mathbf{B}$ drifts. Depending on the exact plasma conditions, different effects become important in balancing the blob polarization and, thus, different regimes of the model are obtained (see e.g. [3, 4, 11–14] and references therein). Just recently, the effects of a finite ion temperature were included into a blob model [15]. For the sheath limited regime, where the blob polarization is balanced by parallel currents across the sheath only, this model predicts the highest growth rate for a blob size δ_* of [15]

$$\delta_* = \rho_\mathrm{s} \left(8(1+\tau_\mathrm{i})\right)^{1/5} \cdot \left(\frac{l_\parallel^2}{\rho_\mathrm{s} R}\right)^{1/5} . \tag{1}$$

Here, $\tau_\mathrm{i} = T_\mathrm{i}/T_\mathrm{e}$ is the ratio of the ion and electron temperature, $l_\parallel$ is the parallel length of the filament, $\rho_\mathrm{s} = \sqrt{m_\mathrm{i} T_\mathrm{e}}/eB$ the drift scale and R the major radius (as a measure of the field line curvature). Since δ_* is the blob size at the largest growth rate, individual blobs can have different sizes δ_b. However, it can be expected that the value of δ_* influences the distribution of δ_b observed in the experiment. The corresponding velocity for the same regime is given by [15]

$$v_{r,\mathrm{b}} = (1+\tau_\mathrm{i}) c_\mathrm{s} \left(\frac{\rho_\mathrm{s}}{\delta_\mathrm{b}}\right)^2 \frac{l_\parallel}{R} . \tag{2}$$

Apart from a prefactor, the equations describing the blob size and radial velocity agree with those from the sheath limited blob model assuming cold ions [3, 16, 17]. Hence, the scaling with δ_b, $l_\parallel$, and ρ_s is the same in both models, but the absolute values are increased by the contribution of the ion pressure, which should be more appropriate for fusion plasmas, where the ion temperature in the SOL can be even higher than the electron temperature [18].

Concerning the blob generation rate, there is no quantitative prediction from blob theory yet. There is, however, experimental evidence from basic plasma and

fusion experiments [17, 19–21] that micro instabilities in the edge, like e. g. drift waves or interchange modes, are involved in the blob generation. These instabilities show a broad frequency band up to the MHz range. Since it is also observed that high amplitude blob events are rare, recent experiments hint to exponential amplitude distributions [22], only a small fraction of the generated events is detected. Hence, depending on the applied detection method, detection rates of a few kHz can be expected.

In this paper, the results of gas-puff imaging (GPI) experiments from ASDEX Upgrade concerning the aforementioned blob properties are presented with special focus on differences in L- and H-mode discharges. The paper is organized as follows: In Sec. 2 the experiments and the setup of the diagnostics are described. Sec. 3 presents the experimental results on the dynamics of the blobs and the detection rate, blob size and velocity obtained from single structure analysis. The key findings of these experiments are summarized in Sec. 4.

2. Experimental setup

The experiments presented in this paper were all performed on ASDEX Upgrade in the magnetic lower single null configuration with a magnetic field strength B_t around $-2.5\,\mathrm{T}$. The toroidal plasma current was $I_\mathrm{p} = 0.8\,\mathrm{MA}$ and the line edge density (i. e. the line averaged density measured by interferometer line H-5, see e.g. [20] for a detailed description of the setup) $\bar{n}_\mathrm{e}$ was about $2 \cdot 10^{19}/\mathrm{m}^3$. These parameters were chosen to obtain comparable discharges to previous measurements of blob dynamics in ASDEX Upgrade presented in Refs. [23–25]. Each discharge consisted of a purely Ohmically heated L-mode phase before additional 3 MW of ECR heating triggered the L-H transition and a stable H-mode was sustained. Due to the lack of T_e-profiles from probe measurements for the analyzed discharges, T_e had to be assumed in the far-SOL for a comparison with the analytical scalings. Thomson data and an outward shift in the emitted intensity suggest a slight increase in T_e in the H-mode phases. This is uncommon for ASDEX Upgrade, but has been observed before [28]. Hence, it is assumed that in the far-SOL, where T_e is nearly constant, $T_\mathrm{e,L} = 15 \pm 5\,\mathrm{eV}$ and $T_\mathrm{e,H} = 20 \pm 5\,\mathrm{eV}$. Furthermore, it is assumed that the ion temperature $T_\mathrm{i} = 3T_\mathrm{e}$, as it is found experimentally at ASDEX Upgrade [18]. These values have to be confirmed in future experiments.

At ASDEX Upgrade the camera is located in a shielding box next to the vacuum vessel for protection against ionizing radiation. The plasma is observed via a mirror inside an immersion tube in the vacuum vessel. The lens system is located close to the mirror and the resulting image is focused on one end of a coherent fibre bundle, which transmits the image to the shielding box. In the shielding box, the fast camera observes the other end of the coherent fibre bundle with a second lens system to capture the image. The resulting camera view observes the far-SOL plasma on the low field side below the midplane ($z = 0$) and is discussed further below. The employed frame rate is 120 kfps (kilo frames per second) at an image resolution of 64×64 pixels and a spatial resolution at the focused plane of about 1 mm/pixel.

The blobs were mainly studied by means of gas-puff imaging (GPI). GPI is a well established technique in many fusion experiments to study edge turbulence (see e. g. [26, 29–33]). A gas puff of typically deuterium or helium is used to locally increase the neutral background pressure. The radiation emitted by the gas cloud as a consequence of collisions of plasma electrons with the neutrals is observed by a

high speed camera (in this case a Phantom v7.3). Figure 1 displays the averaged light intensity recorded by the fast camera in the SOL during a deuterium gas-puff.

As stated above, the observed region is located slightly below the midplane at z=0. With the applied camera settings, only the SOL is observed, i. e. the separatrix ($\rho_{\mathrm{pol}} = 1.0$) is not captured in the imaged region, but is located to the left of it in the representation of Fig. 1, where the dashed lines indicate the positions of $\rho_{\mathrm{pol}} = 1.05$ and $\rho_{\mathrm{pol}} = 1.10$. The maximum intensity is observed close to $\rho_{\mathrm{pol}} \approx 1.065$, which is in the limiter shadow of the heat shield for the L-mode phases, but not for the inter-ELM H-mode phases. The influence of this circumstance on the blob dynamics has to be studied in the future. Technical limitations concerning the positioning of the tube and the mirror lead to a line-of-sight, which is not exactly tangential to the magnetic field lines. Due to the line integration along the line-of-sight this leads to a distortion of the structures in the image data. The effect of the toroidal projection on the determination of velocities from the image data was studied by implementing a synthetic diagnostic: Using field line tracing, field-aligned filaments with a toroidal extension matching the one of the observed light emission of the gas cloud were calculated and observed by a virtual camera. The obtained synthetic images were analyzed using the same image processing methods that are used for the experimental data. The error of the velocities determined from the experimental data can be estimated by comparing the velocities observed in the synthetic camera data to the precisely known velocities of the modeled filaments. It is found that the poloidal velocity is correctly reproduced with an error of less than 10%, while the radial velocity determined from the image data is underestimated by a factor of 1.4. Consequently, the radial velocities reported in the following are corrected by this factor.

Figure 2 shows turbulent structures visible in the GPI after subtracting the mean intensity. Due to their extension along the field lines, the structures appear elongated in the radial direction. Hence, to determine the blob size only the poloidal semi axis of the fitted ellipse is taken as a measure for δ_b. The blob properties were obtained by detecting blobs in the image data and representing the detected structure by an ellipse. Details on the method of blob detection applied can be found in Ref. [21]. The resulting properties are quantitatively comparable to those found by a lithium beam diagnostics [34].

3. Results

This section starts with a discussion of the qualitative blob structure and dynamics in the conditional average of the image data, followed by a presentation of quantitative results concerning the detection rate, cross-field size δ_{b}, and radial velocity $v_{r,\mathrm{b}}$ from a single-structure analysis.

3.1. Dynamics in the conditional average

The conditional average (CA) is commonly used to study the characteristic dynamics of coherent structures in turbulent systems both in experiments and simulations (see e. g. Ref. [35]). In this section, CA results are shown for the deuterium gas-puff, where the emitted light intensity reaches its maximum in front of the limiter near the segment S13. The CA is compared for an L-mode and H-mode phase in the same discharge.

In order to compare turbulent structures over the whole emission range,

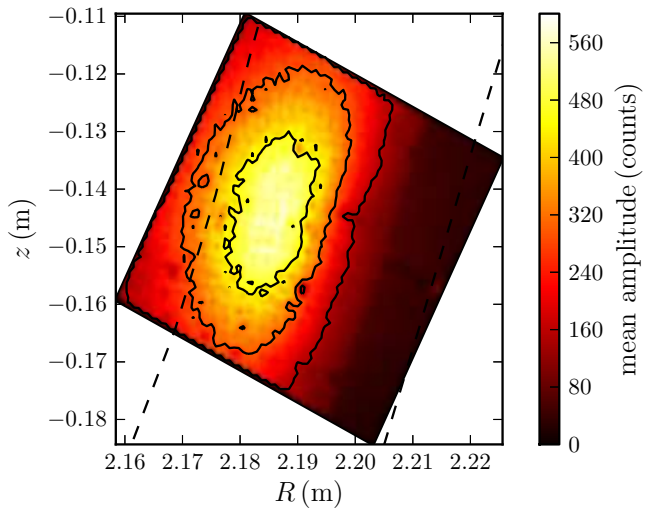

Figure 1. Mean count rate captured by the camera during a deuterium gas-puff. The left dashed line marks the position of $\rho_{\mathrm{pol}} = 1.05$, the right dashed line of $\rho_{\mathrm{pol}} = 1.10$.

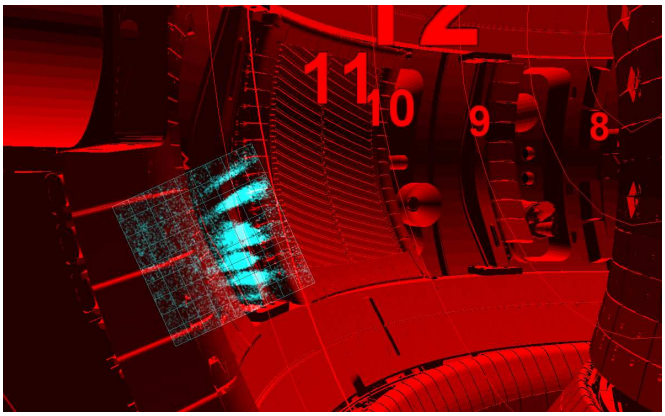

Figure 2. Model of the interior of the ASDEX Upgrade vessel overlayed with a camera image (blue) showing fluctuations in the SOL.

normalized intensity fluctuations $\tilde{I}_n$ are used:

$$\tilde{I}_n = \frac{I - \langle I \rangle}{\langle I \rangle} \,, \tag{3}$$

where I is the intensity recorded by the camera and $\langle I \rangle$ the time average of each individual pixel. Figure 3 shows six time instances of the conditional average (CA) of $\tilde{I}_n$. The reference pixel is marked by the gray cross, the threshold chosen for the CA is two times the standard deviation and a total of 875 trigger events were averaged. The dashed line indicates the position of the limiter mentioned above. The x-axis lies close to the radial direction (ρ), the y-axis close to the poloidal direction (compare Fig. 1

for the exact geometry). A blob is seen in the intensity fluctuations, which propagates radially outwards and poloidally in the electron diamagnetic direction (to the top). The observed (poloidal) structure size is about 10 pixels in the image data, which corresponds to a physical size of $\delta_\mathrm{b} \approx 1\,\mathrm{cm}$. At $\tau = 0\,\mu\mathrm{s}$ (Fig. 3 b) the blob features an elliptical shape, which is elongated in the radial direction due to the integration along the line-of-sight (LOS). Close to the limiter (images d-f), the blob features a more complex shape and develops a tail-like structure, at least in the image data. As a consequence, the blob size and velocity cannot be defined clearly in the vicinity of the limiter and the corresponding region is ignored in the analysis presented below.

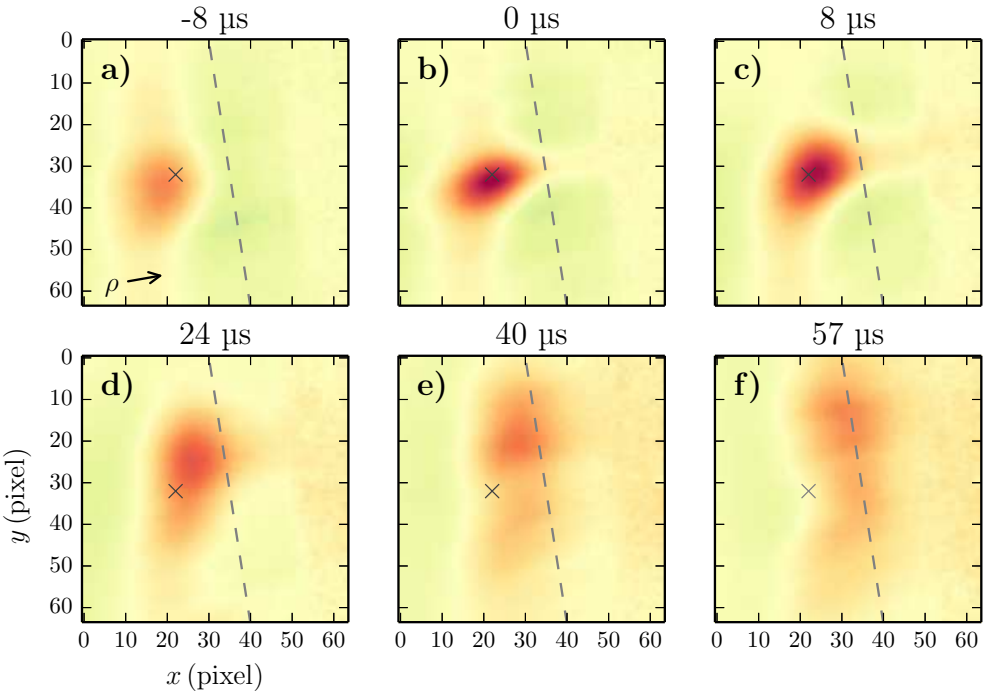

Figure 3. Conditional average of normalized intensity fluctuations $\tilde{I}_n$ recorded during an L-mode phase (875 trigger events). The fluctuation amplitude is scaled to the maximum at t=0, positive values are shown in red, negative ones in blue. The cross (gray) marks the location of the reference pixel, the dashed line (light gray) depicts the limiter at segment S13. The radial direction ρ agrees approximately with the x direction and the poloidal one with the y direction. The exact orientation of the images can be seen in Fig. 1.

Figure 4 shows a CA analysis similar to the one presented above, but this time for blobs observed in the inter-ELM H-mode phases of the same discharge (556 trigger events). A blob is seen in the captured intensity fluctuations, which also propagates radially outwards. But compared to the L-mode case a smaller poloidal velocity is observed, which even points in the opposite direction. This indicates a change in the radial electric field. A similar reversal of the poloidal velocity between L- and H-mode phases is also observed in other devices, e. g. in the stellarator Heliotron J [36]. Also, the blob size appears to be larger at $\tau = 0$ than in the L-mode phase. The analysis of single structures presented below confirms this observation. Apart from

these features (poloidal propagation and size), there are no differences apparent in the CA between L- and inter-ELM H-mode phases of the analyzed discharges concerning the blob properties and dynamics.

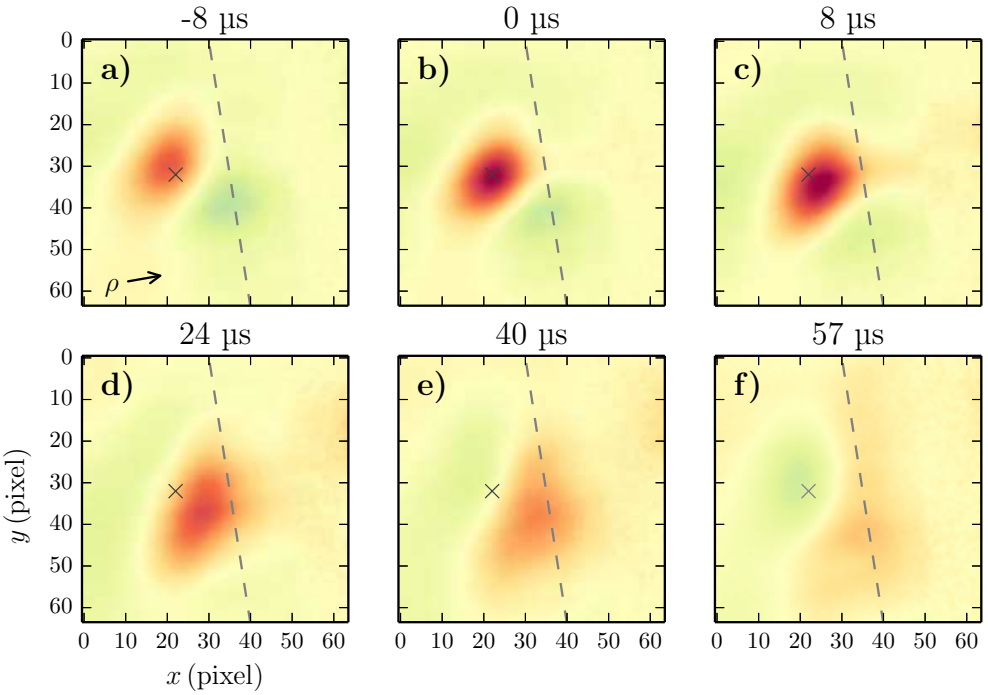

Figure 4. Conditional average of normalized intensity fluctuations $\tilde{I}_n$ recorded during inter-ELM H-mode phases (556 trigger events). The representation is the same as in Fig. 3.

3.2. Detection rate

In Ref. [23] it was observed that blob generation at ASDEX Upgrade takes place approximately 1 cm outside of the nominal separatrix position. Here, the blobs are not detected in this region, but after propagating into the field of view of the camera, where the gas-puff provides sufficiently high light intensities to detect turbulent structures in the SOL. Since there is no indication that blobs appear spontaneously in the far SOL, the detection rate can be used as a proxy of the generation rate, where the accuracy depends on the life time of the blobs and their trajectory.

Blobs were detected in the normalized raw data (according to Eq. (3)) by using the object recognition method. A cluster of pixels with high amplitudes is related to a blob if the peak amplitude is larger than the standard deviation and the cluster consists of more than 20 pixels detecting at least half of the peak amplitude. This *area threshold* is introduced to prevent spurious blob detection due to noise. To determine how frequently blobs occur in the field of view, a square of 10×10 pixels is defined as detection region and is chosen such that no structures are truncated at the image edges or interact with the limiter (see Sec. 3.1). The detection time t_i of an individual

structure i is defined as the time when the center of mass of the normalized intensity fluctuations associated with the blob enters the detection region. Tracking the single structures over several images prevents multiple counting of the same structure. As a result, the detection rates are obtained and also the waiting-time distribution (WTD), i. e. the distribution of observed *waiting times* between subsequent structures defined as $t_\mathrm{w} = t_i - t_{i-1}$.

The resulting WTDs for an L-mode phase and inter-ELM H-mode phases are compared in Fig. 5. Since the datasets cover time intervals of different length, the count rate per waiting-time interval is normalized to the total amount of observed blobs. The corresponding detection rates are 3320 blobs/s for the L-mode phase and 4416 blobs/s for the inter-ELM H-mode phases. The shape of the WTDs and the detection rates

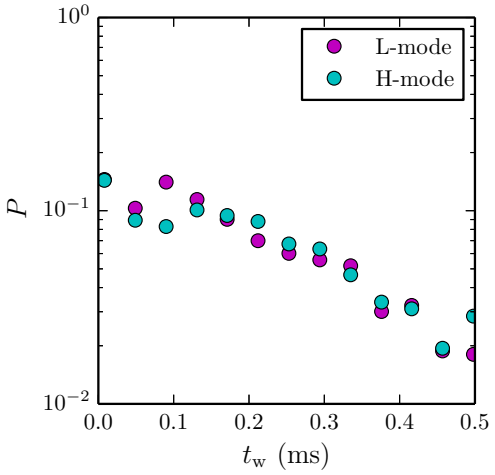

Figure 5. Comparison of waiting-time distributions for blobs observed during a deuterium gas-puff in an L-mode phase and inter-ELM H-mode phases of #28769. The error is within the symbol size.

compare well for both phases, which indicates that the blob generation mechanism does not change fundamentally. The slight increase in the detection rate observed in the inter-ELM H-mode phases does not necessarily indicate a larger generation rate: Due to the larger average blob size (see Sec. 3.3) more blobs exceed the area threshold introduced above. The result does not depend on the detection area selected.

3.3. Blob size

The poloidal blob sizes have been deduced from the image data recorded during deuterium gas-puffs in L- and inter-ELM H-mode phases of different discharges. The sizes of blobs with a center of mass detected in the region between the radial positions $R = 2.175$ and 2.180 m and the vertical positions $z = -0.15$ and -0.145 m (around $\rho_\mathrm{pol} = 1.07$) are averaged. Two sample blob size distributions obtained for the L-mode phase of #28769 (a) and inter-ELM H-mode phases (b) of the same discharge are shown in Fig. 6. The average size in the L-mode phase is $\delta_\mathrm{b} = 6.8 \pm 0.1$ mm and in the inter-ELM H-mode phases $\delta_\mathrm{b} = 8.2 \pm 0.1$ mm. The steep edge of the blob size distribution for the L-mode blobs left of the maximum indicates that there are blobs with a δ_b smaller than 4 mm, which are not properly resolved due to the resolution of

the optical setup and the area threshold of the blob detection algorithm. Hence, the mean value of δ_b obtained from the camera data may be overestimated.

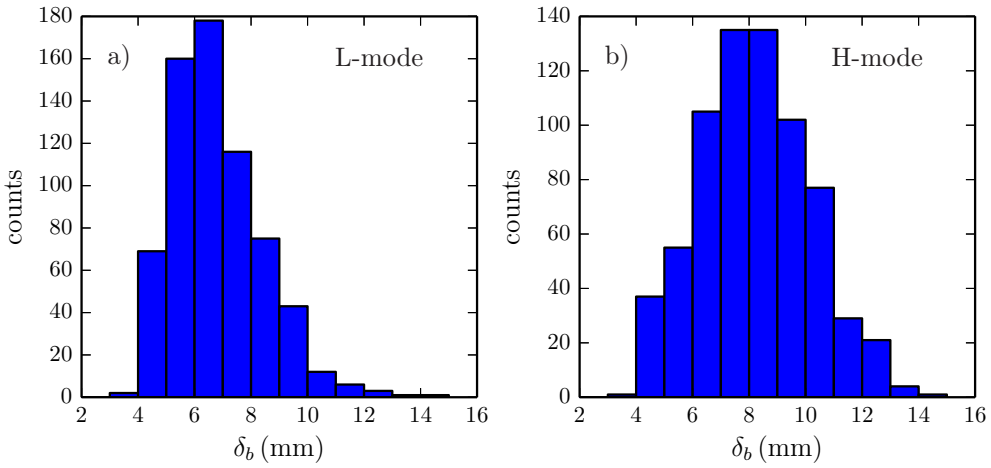

Figure 6. Size distribution (δ_b) for blobs around $\rho_\mathrm{pol} = 1.07$ in L-mode phases (a) and inter-ELM H-mode phases (b) of the same discharge.

Nevertheless, by comparing both the mean value of δ_b and the maxima in the size distributions it can be concluded that δ_b is increased in the inter-ELM H-mode phases, which is in agreement with the CA results shown above. However, the change in δ_b of roughly 20 % is small and is even smaller in another analyzed discharge (#28768), where δ_b is 6.4 ± 0.2 mm in the L-mode phase and 7.2 ± 0.1 mm in the inter ELM H-mode phases. Note that since GPI does not provide a direct density measurement, it is not clear if the observed small changes can directly be related to changes in the size of the density perturbation associated with the blobs.

Fig. 7 shows a comparison of the experimental values with a) the Krasheninnikov scaling [3] for the case $T_\mathrm{i} = 0$ and b) predictions by the warm-ion scaling Eq. (1) for the case $T_\mathrm{i} = 3T_\mathrm{e}$. The two scaling laws are identical apart from a factor of $8(1+\tau_\mathrm{i})^{1/5}$ and are evaluated using the following parameters for the observed region: $R = 2.18$ m, $B = 1.9$ T, and $l_\parallel = 5$ m. With both choices blob sizes of the right order of magnitude are predicted. The inclusion of finite ion temperature effects improves the agreement.

3.4. Blob velocity

From the dynamics apparent in the CA it can be anticipated that there is no drastic change in the radial blob velocity in L- and H-mode phases of the analyzed discharges. This is quantified in this section by analysing the dynamics of single structures, using the object recognition method, and tracking the individual blobs over several images. The velocities of all structures with the same center of mass position are then averaged to obtain a spatially resolved characteristic velocity field. Using the poloidal magnetic flux Ψ_p from the magnetic reconstruction, the radial (parallel to the gradient of the poloidal flux $\nabla\Psi_\mathrm{p}$) and poloidal (perpendicular to $\nabla\Psi_\mathrm{p}$ and $\mathbf{B}$) velocity can be determined. The spatially resolved poloidal velocity field is compared in Fig. 8 for the L-mode (a) and inter-ELM H-mode (b) phases of the same discharge. While

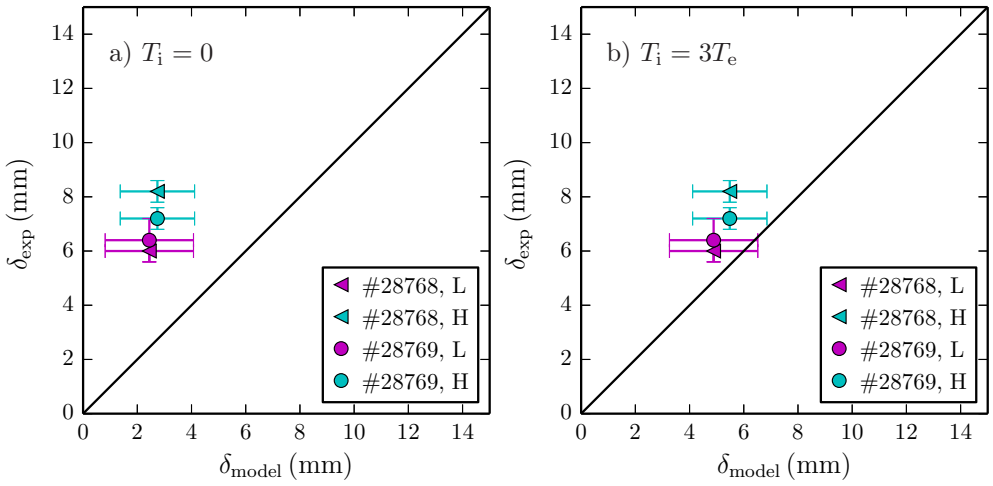

Figure 7. Comparison of the average blob size δ_{exp} with the prediction δ_{model} from a cold ion model (a) and a warm ion model (b).

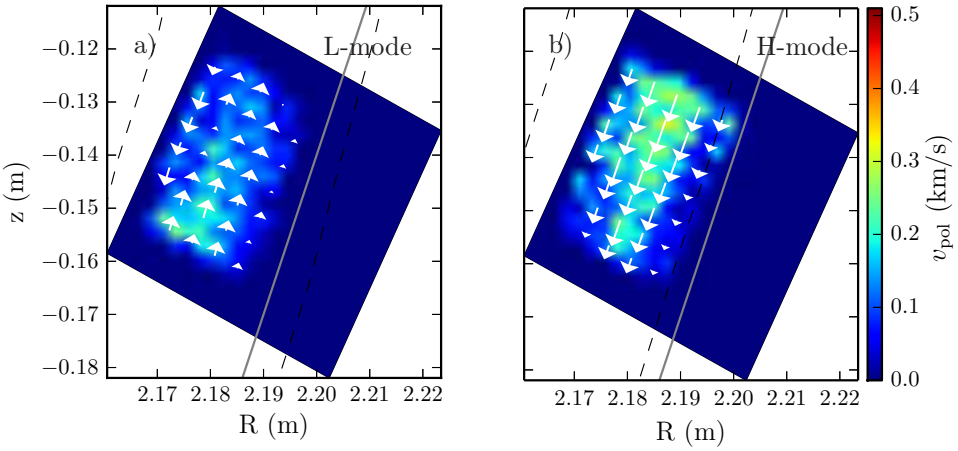

Figure 8. Poloidal velocity fields obtained from camera data during a deuterium gas puff in an L-mode phase (a) and inter-ELM H-mode phases (b) of the same discharge. The left dashed line marks $\rho_{pol} = 1.05$, the right one $\rho_{pol} = 1.10$. The closed line (gray) marks the location of the limiter.

the absolute values are comparable in both phases, between 100 and 300 m/s with a tendency to larger values in the H-mode phase, there is a clear reversal in the poloidal propagation direction. Assuming that the poloidal velocity is mainly determined by the $\mathbf{E} \times \mathbf{B}$ background drift, this result suggests the possibility for complex changes in the radial electric field after the L-H transition. Similar features are also observed in other devices, e. g. in Heliotron J [36]. Implications of poloidal velocity shear layers for the dynamics of blobs are discussed in Refs. [25–27].

The radial velocity fields are shown in Fig. 9, again for the L-mode (a) and inter-ELM H-mode (b) phases of one shot. Both velocity fields compare well, showing a

decrease of the radial velocity in the radial direction from about 200 m/s at the inner edge of the observed region to zero in front of the limiter. A comparable behaviour is documented for DIII-D in Ref. [5] and was assumed for ASDEX Upgrade, to explain observations from ion-temperature measurements [18] and measured with Langmuir probes [37]. This observation can be explained by the blob model due to parallel pressure losses to the walls. Furthermore, it is observed that, apart from the region close to the limiter, the radial velocity at a given location is slightly larger in the L-mode phase. This would qualitatively agree with the expectation from Eq. (2), which predicts a decreasing radial velocity with increasing blob size at otherwise unchanged plasma conditions. For a quantitative comparison the radial velocities are averaged

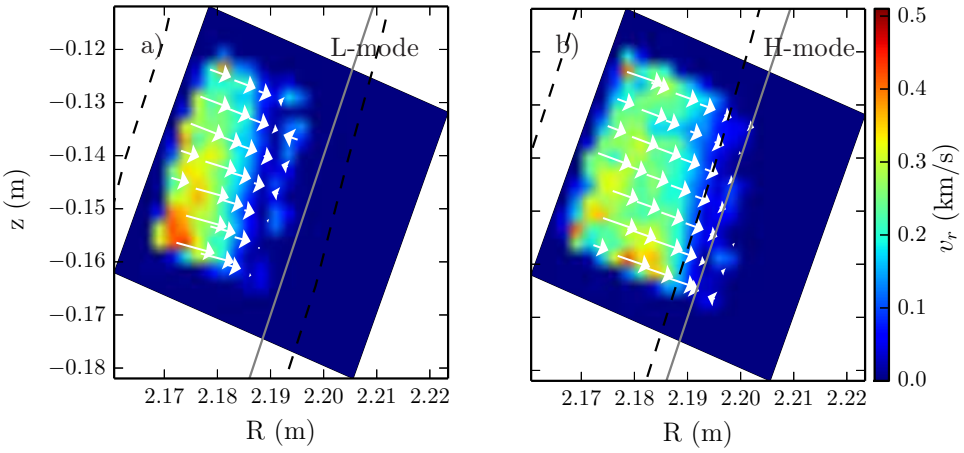

Figure 9. Radial velocity fields obtained in an L-mode phase (a) and inter-ELM H-mode phases (b). The representation is the same as in Fig. 8.

in the same region as the blob sizes above. In Fig. 10 the results are compared to predictions from analytical scaling laws. Again, in the observed region ($R = 2.18$ m, $B = 1.9$ T and $l_{\parallel} = 5$ m) the Krasheninnikov scaling [3] is employed for a) $T_\mathrm{i} = 0$ and the warm-ion scaling Eq. (2) for b) $T_\mathrm{i} = 3T_\mathrm{e}$. Both scalings predict velocities of the right order of magnitude. For $\tau_\mathrm{i} = 0$ the predicted velocity is smaller than the observed value, while for $T_\mathrm{i} = 3T_\mathrm{e}$ the prediction is slightly larger. Due to the ρ_s^2 dependence of the radial velocity and the fact that the temperature in the far-SOL had to be assumed, the error bars of the theoretical prediction are large. Future experiments will investigate this discrepancy in more detail by comparing different diagnostics and building up a larger data base. According to the observed density and temperature profiles, collisional scalings like those presented in Refs. [11, 15] should not apply, since the collision parameter Λ is smaller than 1. It is, however, apparent from other experiments [38], that the background n_e influences the blob velocity, indicating that not all relevant physics may be considered in the theoretical scaling deployed here.

4. Summary and conclusion

Fast camera measurements in the SOL of ASDEX Upgrade were performed using the technique of gas-puff imaging. All discharges started as purely Ohmically heated L-

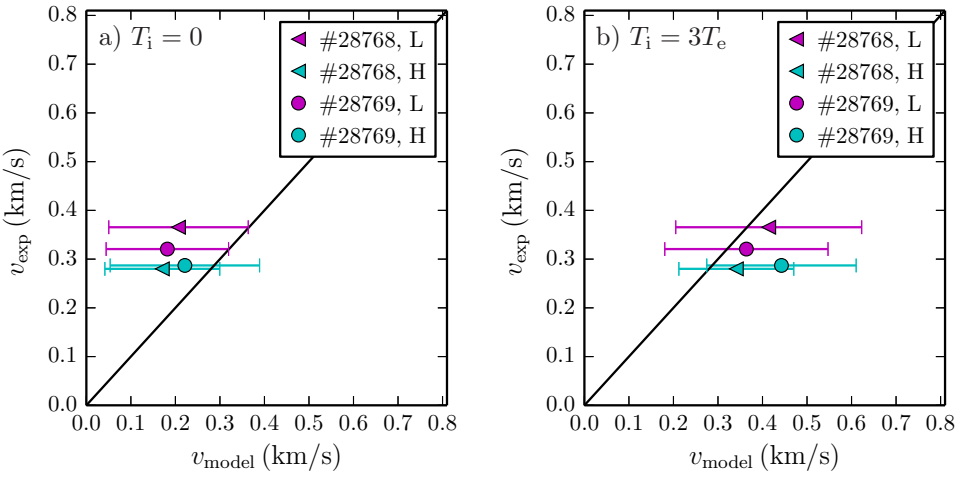

Figure 10. Comparison of averaged radial blob velocities (v_exp) with a cold ion model (a) and a warm ion model (b).

mode plasmas before additional ECRH triggered the L-H transition. Hence, it was possible to compare the blob detection rate, size δ_b, and velocity (poloidal and radial) for L- and inter ELM H-mode phases. Although the edge plasma parameters change drastically from L to H-mode, only small changes in the blob dynamics were observed. This is in line with the observations reported from Alcator C-Mod [9] and DIII-D [7].

It was observed that the blobs in H-mode are larger in size and that they have a smaller radial outward velocity. Both changes are, however, not as striking as to indicate a dramatic change in the blob dynamics between L- and H-mode. A similar trend (larger poloidal blob sizes and only slightly changed radial velocity) is reported from MAST [39]. In accordance with these results is the observation that the detection rate and waiting-time distribution (WTD) remain almost unchanged after the L-H transition. The detection rate is slightly increased in H-mode. However, since the detection rate depends on the blob size and amplitude it cannot be decided if the increase in the detection rate also reflects changes in the generation rate of blobs. It is in any case remarkable, how little the change in the detection rates is. This indicates that the turbulent dynamics just around the separatrix, which is likely responsible for blob generation, may be unaffected by the striking changes in the edge parameters comparing L- and H-mode plasmas [40].

Furthermore, the camera measurements revealed in both confinement regimes a deceleration of the radial blob velocity $v_{r,\mathrm{b}}$, while the blobs propagate outwards.

The only significant change in the blob dynamics between the L- and H-mode phase were observed in the poloidal velocity profiles. In the outer SOL ($\rho_\mathrm{pol} \gtrsim 1.06$) the poloidal propagation is reversed.

The experimentally observed values for δ_b and $v_{r,\mathrm{b}}$ were compared to a novel blob model including warm-ion effects [15]. A good agreement with this model was found for the blob sizes. The predicted velocities, however, are slightly too large. Future experiments will build up a larger data base and focus on a multi-diagnostic approach in order to get reliable temperature measurements in the far-SOL and to get an even better understanding of what influences the radial velocity of blobs in the SOL of fusion

experiments. If the theoretical blob size and velocity scaling laws indeed describe the observed blob dynamics, as it is reported here for ASDEX Upgrade and also for many other experiments (see especially [4] for an extensive review), this could explain their similarity in the different confinement regimes: If the SOL plasma parameters stay approximately constant, also the blob size and velocity are comparable. Since there is no quantitative prediction for the generation/detection rate yet, no such conclusion can be drawn for the similarity of the detection rate reported in this paper and for Alcator C-Mod [9].

In conclusion, the fact that the strong suppression of turbulence in the H-mode edge plasma, compared to L-mode phases, is not reflected in blob transport, casts some light on the blob production mechanism and could be explained if the blobs are not generated in the edge but further out, maybe at the separatrix. In probe measurements [23, 25] a generation of blobs about 1 cm outside the nominal separatrix of ASDEX Upgrade was found. The validation of the blob model was partially successful, but additional experiments are needed. While the blob sizes agree rather well with a blob model taking finite ion temperatures into account [15] the results on the radial velocity are promising, however not yet conclusive.

5. Acknowledgments

This project has received funding from the Euratom research and training programme 2014-2018.

References

[1] Wagner F *et al* 1982 *Phys. Rev. Lett.* **49** 1408

[2] Zweben S J 1985 *Phys. Fluids* **28** 974

[3] Krasheninnikov S I, D'Ippolito D A and Myra J R 2008 *J. Plasma Phys.* **74** 679

[4] D'Ippolito D A, Myra J R and Zweben S J 2011 *Phys. Plasmas* **18** 60501

[5] Boedo J A *et al* 2001 *Phys. Plasmas* **8** 4826

[6] LaBombard B, Boivin R L, Greenwald M, Hughes J, Lipschultz B, Mossessian D, Pitcher C S, Terry J L, Zweben S J and Alcator Group 2001 *Phys. Plasmas* **8** 2107

[7] Rudakov D L *et al* 2002 *Plasma Phys. Control. Fusion* **44** 717

[8] LaBombard B *et al* 2004 *Nucl. Fusion* **44** 1047

[9] Terry J L *et al* 2005 *Nucl. Fusion* **45** 1321

[10] Cziegler I, Terry J L, Hughes J W and LaBombard B 2010 *Phys. Plasmas* **17** 056120

[11] Myra J R, D'Ippolito D A, Stotler D P, Zweben S J, LeBlanc B P, Menard J E, Maqueda R J and Boedo J 2006 *Phys. Plasmas* **13** 092509

[12] Garcia O E, Bian N H, Naulin V, Nielsen A H and Juul Rasmussen J 2005 *Phys. Plasmas* **12** 090701

[13] Katz N, Egedal J, Fox W, Le A and Porkolab M 2008 *Phys. Rev. Lett.* **101** 015003

[14] Theiler C, Furno I, Ricci P, Fasoli A, Labit B, Müller S H and Plyushchev G, 2009 *Phys. Rev. Lett.* **103** 65001

[15] Manz P, Carralero D, Birkenmeier G and Müller H W and Müller S H, Fuchert G, Scott B D and Stroth U 2013 *Phys. Plasmas* **20** 102307

[16] D'Ippolito D A, Myra J R and Krasheninnikov S I 2002 *Phys. Plasmas* **9** 222

[17] Krasheninnikov S I 2001 *Phys. Lett. A* **283** 368

[18] Kočan M, Gennrich F P, Kendl A, Müller H W and the ASDEX Upgrade Team 2012 *Plasma Phys. Control. Fusion* **54** 085009

[19] Antar G Y 2003 *Phys. Plasmas* **10** 3629

[20] Carralero D, Shoji M, de la Cal E, van Milligen B Ph, de Pablos J L, Hidalgo C and Yamada H 2011 *Contrib. Plasma Phys.* **51** 92

[21] Fuchert G, Birkenmeier G, Nold B, Ramisch M and Stroth U 2013 *Plasma Phys. Control. Fusion* **55** 125002

[22] Garcia O E, Fritzner S M, Cziegler I, Kube R, Cziegler I, LaBombard B and Terry J L 2013 *Phys. Plasmas* **20** 055901

[23] Nold B, Conway G D, Happel T, Müller H W, Ramisch M, Rohde V, Stroth U and the ASDEX Upgrade Team 2010 *Plasma Phys. Control. Fusion* **52** 065005

[24] Nold B, Ribeiro T T, Ramisch M, Huang Z, Müller H W, Scott B D, Stroth U and the ASDEX Upgrade Team 2012 *New J. Phys.* **14** 063022

[25] Nold B *et al*, to be published

[26] Terry J L, Zweben S J, Umansky M V, Cziegler I, Grulke O, LaBombard B and Stotler D P 2009 *J. Nucl. Mater.* **390** 339

[27] Myra J R, Davis W M, D'Ippolito D A, LaBombard B, Russel D A, Terry J L and Zweben S J 2013 *Nucl. Fusion* **53** 073013

[28] Neuhauser J et al 2002 *Plasma Phys. Control. Fusion* **44** 855

[29] Goodall D H J 1982 *J. Nucl. Mater.* **111-112** 11

[30] Zweben S J *et al* 2004 *Nucl. Fusion* **44** 134

[31] Cziegler I, Diamond P H, Fedorczak N, Manz P, Tynan G R, Xu M, Churchill R M, Hubbard A E, Lipschultz B, Sierchio J M, Terry J L and Theiler C 2013 *Phys. Plasmas* **20** 055904

[32] Shao L M *et al* 2013 *Plasma Phys. Control. Fusion* **55** 105006

[33] Xu G S *et al* 2014 *Nucl. Fusion* **54** 013007

[34] Birkenmeier G, Laggner F M, Willensdorfer M, Kobayashi T, Manz P, Wolfrum E, Carralero D, Fischer R, Sieglin B, Fuchert G, Stroth U and ASDEX Upgrade Team 2014 *Plasma Phys. Control. Fusion* **56** 075019

[35] Johnsen H, Pécseli H L and Trulsen J 1987 *Phys. Fluids* **30** 2239

[36] Nishino N, Mizuuchi T, Kobayashi S, Nagasaki K, Okada H, Sano F, Yamamoto S and Kondo K 2008 *Plasma Fusion Res.* **3** S1023

[37] Müller H W, Carralero D, Birkenmeier G, Conway G D, Fischer R, Happel T, Manz P, Suttrop W, Wolfrum E and the ASDEX Upgrade Team 2014 *Contrib. Plasma Phys.* **54** 261

[38] Carralero D *et al*, *to be published*

[39] Ben Ayed N, Kirk A, Dudson B, Tallents S, Vann R G L, Wilson R and the MAST team 2009 *Plasma Phys. Control. Fusion* **51** 035016

[40] Happel T, Estrada T, Blanco E, Hidalgo C, Conway G D, Stroth, U and TJ-II Team 2011 *Phys. Plasmas* **18** 102302

[41] Horton L D, Chankin A V, Chen Y P, Conway G D, Coster D P, Eich T, Kaveeva E and Konz C, Kurzan B, Neuhauser J, Nunes I, Reich M, Rozhansky V, Saarelma S, Schirmer J, Schweinzer J, Voskoboynikov S, Wolfrum E and the ASDEX Upgrade Team 2005 *Nucl. Fusion* **45** 856